CHEMISTRY OF MATERIALS

Article

pubs.acs.org/cm

Elucidating the Role of Defects for Electrochemical Intercalation in Sodium Vanadium Oxide

Evan Uchaker, Hongyun Jin, Pei Yi, and Guozhong Cao*

Department of Materials Science & Engineering, University of Washington, Seattle, Washington 98195, United States

Supporting Information

ABSTRACT: $Na_{1.25+x}V_3O_8$ (with $x < 0$, $= 0$, and > 0) was synthesized via a wet chemical route involving the reduction of V_2O_5 in oxalic acid and $NaNO_3$ followed by calcination. It was possible to control the sodium composition in the final product by adjusting the amount of sodium precursor added during synthesis. It was revealed that deficient and excessive sodium contents, with respect to the ideal stoichiometry, are accommodated or compensated by the respective generation of oxygen vacancies and partial transition metal reduction, or cation disordering. When examined as NIB electrode material, the superior performance of the cation disordered material with excessive sodium was clearly demonstrated, with more than 50% higher storage capacity and superior rate capacity and cyclic stability. The formation of oxygen vacancies initially seemed promising but was coupled with stability issues and capacity fading upon further cycling. The disparity in electrochemical performance was attributed to variations in the electronic distribution as promoted through Na−ion interactions and the direct influence of such on the oxygen framework (sublattice); these factors were determined to have significant impact on the migration energy and diffusion barriers.

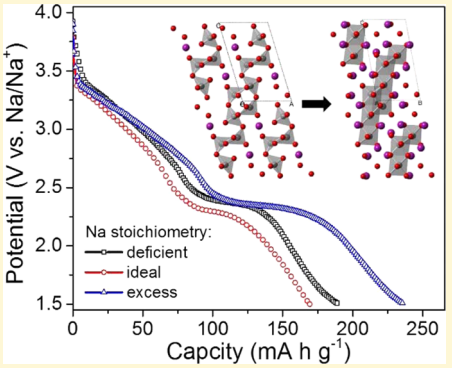

INTRODUCTION

The proliferation of electrical energy demand has driven the rapid progression of improved technologies related to energy distribution and storage. However, energy storage materials and devices have come to be viewed as a crux impeding advanced device development. Lithium-ion (Li-ion) batteries are a mature and robust technology because of their high energy density and portability. Despite their success in such application, Li-ion batteries (LIBs) are a poorly suited choice for large-scale energy storage applications given their high cost, associated with resource scarcity, as well as safety concerns. Conversely, sodium-ion (Na-ion) batteries have been gaining considerable traction as a realistic candidate for large-scale energy storage applications over the past several years.

Na-ion batteries (NIB) are attractive because sodium resources are seemingly inexhaustible as well as ubiquitous and, therefore, cost considerably less (by a factor of roughly 30−40 times) than lithium; additionally, sodium does not undergo an alloying reaction with aluminum at low voltage, as is the case with lithium, meaning that aluminum can replace copper as the anodic current collector, which equates to an overall cell cost savings of ∼2%.[1,2] The lower operating voltage of Na-ion cells results in enhanced stability of the nonaqueous electrolyte but also manifests itself in lower energy density. The majority of the proposed electrode materials for Na-ion battery show similar or slightly lower specific capacity and redox potential than when used in Li-ion cells. Moreover, the accommodation of sodium in traditional host materials is difficult because the ionic radius and reduction potential of sodium are strikingly larger than that of lithium. Therefore, the de/sodiation process induces large distortions in the host lattice that ultimately lead to pulverization of the electrode and the impending failure of the cell.[3]

The majority of investigations to date examining Na-ion battery cathodes have focused on intercalation based materials, particularly layered transition metal oxides. The overall process of electrochemical intercalation can be broken down into three simultaneous and sequential processes: (i) redox reactions at the electrode−electrolyte interface, (ii) nucleation and growth of the new interfacial phase, and (iii) charge and mass transfer. Within the layered transition metal oxide paradigm, vanadium oxide is an attractive multifunctional material used for widespread application in various fields such as catalysis and energy storage. Of the many stoichiometries and polymorphs, sodium trivanadate, $Na_xV_3O_8$, is a propitious positive electrode material for alkali-ion insertion because of its low cost, easy synthesis, and solid electrochemical performance. This oxide has a layered structure, with the anionic V_3O_8 layers held together by alkali ions, typically Li^+ or Na^+, which have respective theoretical capacities of 372 and 352 mA h g^{-1} when cycled against their constituent metal.

Simple defect modification is a powerful means toward improving material intercalation capabilities that has been receiving considerable interest lately as it can directly alter both

Received: July 29, 2015
Revised: October 1, 2015
Published: October 8, 2015

DOI: 10.1021/acs.chemmater.5b02935
Chem. Mater. 2015, 27, 7082−7090

chemical and structural characteristics; techniques of note include cationic disordering, amorphization, doping, partial cation reduction, and manipulation of intrinsic defects (e.g., oxygen vacancies, denoted V_O in the Kröger−Vink notation).[4−12] Surface defects can directly impact alkali-ion intercalation by shifting the thermodynamics and improving kinetics.[13] The presence of surface defects increases the surface energy and can potentially serve as nucleation sites that facilitate the electrochemical phase transition. Surface-reaction-limited dynamics predict the phase boundary extends from surface to surface along planes of fast ionic diffusion where defects or facet edges can act as nucleation sites.[14] Such results have been verified experimentally, where defects have been reported to promote the phase transition of TiO_2 by providing low energy mass transport routes during the phase transition process.[15,16] Defects may also reduce the stress and the electrostatic repulsion between adjacent oxygen layers, which can directly alter the migration energy and diffusion barriers the alkali ion must overcome during intercalation.[17]

Disordering has been shown to increase the solid solution behavior, reduce the two-phase transformation domains, lower the alkali-ion extraction energy, and modify the diffusion/transport properties during the de/intercalation processes;[4,18−23] the use of amorphous structures is proposed to work in a similar manner while providing a more open framework for ion migration.[5,24−27] Cation disorder involves the intermixing between the alkali ion and the transition metal sublattice and is more likely to exist in systems where there are different redox sites, be it in the form of several transition metal elements or a single multivalent element. Doping is often used as a technique to achieve partial cation reduction, although the later can be successfully done without such means, to introduce mixed valence states in the transition metal and, thus, tune the electronic transport properties of the material.[28] Mixed conductivity, both electronic and ionic, is necessary at the atomic scale for charge neutrality preservation during alkali-ion transport where the chemical diffusion coefficient is ultimately rate-limited by the slower of the two processes. The introduction of oxygen vacancies is well known for increasing conductivity in oxide materials.[29,30] Supervalent metal doping in $LiFePO_4$ was shown to increase the electronic conductivity of by a factor of $\sim 10^8$, effectively overcoming the low intrinsic limitations of the material.[31]

Several studies have been devoted to examining the effects of lithium nonstoichiometry in LIB electrodes, particularly for $LiCoO_2$ where such effects are accommodated by oxygen vacancies that can also be accompanied by either cation mixing or perturbation of the oxygen stacking layers. Accordingly, the local environment of some cobalt ions can be modified by the presence of the oxygen vacancies. The structure of these lithium overstoichiometric compounds makes them more stable against the de/lithiation process and is a beneficial approach toward preventing structural distortion and, thus, demonstrate potential for LIB electrode development.[32,33] Notwithstanding, the recent rejuvenation in NIB research activity has revealed, if nothing else, that analogous materials can behave substantially different than expected based off their prior LIB performance.[34] There have been minimal reports concerning the role of defects on NIB electrode materials and the potential impact they may have on the overall electrochemical performance.[35,36] Toward these ends, we propose synthesizing $Na_xV_3O_8$ with oxygen vacancies and partial cation reduction by adjusting the sodium stoichiometry to induce the formation of such defects. Structural as well as chemical analyses were conducted to verify the presence of these defects, and the electrochemical performance of the corresponding materials was evaluated as positive electrode material for NIB application.

EXPERIMENTAL PROCEDURE

Material Synthesis. All chemicals were analytical grade and used as received without further processing. Approximately 0.90 g of V_2O_5 (99.8%, Alfa Aesar) and 1.33 g of oxalic acid (Sigma-Aldrich) were incorporated into 40 mL of deionized water and stirred at room temperature until the formation of a clear blue solution was noted, indicating the formation of vanadium oxalate. The reaction can be expressed as follows:

$$V_2O_5 + 3H_2C_2O_4 \rightarrow 2VOC_2O_4 + 2CO_2 + 3H_2O \quad (1)$$

Subsequently, various amounts of $NaNO_3$ (99.995%, Aldrich) were added to the VOC_2O_4 solution under stirring for 1 h in order to control the sodium content. Three stoichiometric quantities of $NaNO_3$ corresponding to sodium contents of 0.75, 1.0, and 1.25, where 1.0 is the ideal stoichiometry of $Na_{1.25}V_3O_8$, were then added. The solution was dried at 80 °C before calcination at 400 °C under ambient for 3 h. The obtained materials were designated as deficient ($Na_{1.25x}V_3O_8$, $x < 1$), stoichiometric ($Na_{1.25x}V_3O_8$, $x = 1$), and excessive ($Na_{1.25x}V_3O_8$, $x > 1$) as based on their stoichiometric sodium concentration.

Characterization. Microscopy investigations were carried out using a FEI Sirion scanning electron microscope (SEM). Nitrogen sorption was performed using a Quantachrome NOVA 4200e. The specific surface area, micropore, and mesopore volumes were determined using multipoint Brunauer−Emmett−Teller (BET), *t*-method, and Barrett−Joyner−Halenda (BJH) desorption analyses, respectively. Thermogravimetric analysis (TGA) was conducted from room temperature to 600 °C (PerkinElmer TGA 7) under nitrogen flow at a heating rate of 5 °C min^{-1}. The phase of the calcined sodium vanadium oxides was studied using X-ray diffraction (XRD, D8 Bruker X-ray diffractometer) with Cu Kα radiation over the range of 10° to 70° (2θ), a step size of 0.02°, and an exposure time of 10 s. The accelerating voltage and current were 40 kV and 40 mA, respectively. The corresponding Rietveld refinement for each pattern was carried out using the GSAS package.[37] The intensities of all the spectra were normalized to the highest intensity peak. Infrared absorption spectra were recorded using a PerkinElmer 1640 Fourier Transform Infrared (FTIR) Spectrophotometer with ATR. X-ray photoelectron spectroscopy (XPS) was completed using a Surface Science Instruments S-probe spectrometer. The X-ray spot size was 800 × 800 μm and the takeoff angle was 55°, corresponding to a sampling depth of approximately 50−70 Å. XPS data analysis was carried out using the Service Physics ESCA 2000-A analysis program (Service Physics, Bend, OR).

Electrochemical Analysis. An electrode slurry was prepared by mixing the synthesized $Na_xV_3O_8$ powders, carbon black (Cabot Vulcan XC72R), and poly(vinylidene fluoride) (PVDF, MTI) binder dispersed in an *N*-methyl-2-pyrrolidone (NMP, Alfa Aesar) solution at a respective weight ratio of 80:12:8. The slurry was spread onto aluminum foil (99.3%, MTI) and dried in a vacuum oven at 80 °C overnight prior to coin-cell assembly. For electrochemical analysis, 2032 half-cells (Hoshen) were assembled in a glovebox (M Braun) filled with high purity argon. Metallic sodium (Sigma-Aldrich), 1 M $NaClO_4$ (98%, Sigma-Aldrich) in ethylene carbonate (BASF)/

DOI: 10.1021/acs.chemmater.5b02935
Chem. Mater. 2015, 27, 7082−7090

Table 1. Physical Properties of $Na_xV_3O_8$ Products with Deficient, Ideal, and Excess Sodium Stoichiometry

				Na content (at %)		XPS Na:V ratio	
sample	water (wt %)	BET surface area (m^2 g^{-1})	BJH pore size (nm)	calculated	EDX	stoichiometric	average
excess	0.26	13.42	3.20	11.60	10.30	0.52	0.49
stoichiometric	0.48	11.41	3.18	9.28	9.06	0.42	0.38
deficient	0.70	8.93	3.18	6.96	6.87	0.32	0.31

propylene carbonate (anhydrous 99.7%, Sigma-Aldrich) (1:1 vol.), and Whatman GF/A glass microfiber filter were used as the counter/reference electrode, electrolyte, and separator, respectively. Cyclic voltammetry (CV) was completed using an electrochemical analyzer (CH Instruments, Model 605C) in the potential range of 4.0−1.5 V (vs Na/Na^+) at scan rates ranging from 0.01 to 10.0 mV s^{-1}. The current density and cycle stability performance of the electrodes were evaluated using a BT-2000 Arbin Battery Tester operating at room temperature. The half-cells were tested within the potential range of 4.0−1.5 V vs Na/Na^+ at various charging rates based on the weight of the active material alone and assuming a 1C current density of 350 mA g^{-1} corresponding to the total accommodation of four sodium ions per $[V_3O_8]$ formula unit.

RESULTS AND DISCUSSION

The chemical synthesis procedure utilized in this investigation allowed for the direct control, within certain constraints, of the sodium content. Thus, by adjusting the amount of $NaNO_3$ precursor added to the VOC_2O_4 solution it was possible to attain $Na_xV_3O_8$ products with deficient, ideal, and excess sodium stoichiometry. A moderately low calcination temperature (400 °C) was employed in order to preserve the purity and structural integrity of the material. When calcined at temperatures higher than 525 °C a NaV_6O_{15} secondary phase would form, as determined through Rietveld refinement, that exhibits markedly lower kinetics toward sodium ions.[38] Sodium plays a significant role in stabilizing the interlayer structure, and the implementation of a high temperature thermal treatment profile to affect the hydration level can result in collapse of the interlayer structure.[39]

TGA was performed to verify that sodium content deficiency was not compensated by hydration or hydrogenation, as was the case for $Na_xV_2O_5{\cdot}nH_2O$, where the water content was found to be inversely proportional to the sodium level.[39] The deficient, stoichiometric, and excess Na samples were revealed to have considerably low water contents of 0.70, 0.48, and 0.26%, substantiating that sodium level manipulation was not compensated through a secondary mechanism (shown numerically in Table 1 and graphically in Figure S1 in Supporting Information (SI)). Nitrogen adsorption−desorption isotherms were collected in order to evaluate the surface area and pore characteristics. The BJH pore size distribution obtained from the nitrogen adsorption−desorption isotherms suggests that the $Na_xV_3O_8$ samples contain broadly distributed pores with sizes below 15 nm, as listed in Table 1 and displayed in Figure S1 in SI, the majority of which are in the 2−5 nm size range. The BET specific surface area was approximated to be 8.9, 11.4, and 13.4 m^2 g^{-1} for the deficient, stoichiometric, and excessive Na samples which are reasonable values for materials containing pores on the aforementioned scale. The moderate surface area of the prepared $Na_xV_3O_8$ materials ensures short alkali-ion diffusion distances and, therefore, holds the potential for enhanced electrochemical performance.

The morphology of the $Na_xV_3O_8$ compounds following calcination was observed by SEM, the micrographs of which are shown in Figure 1a−c. Comparison of the different samples

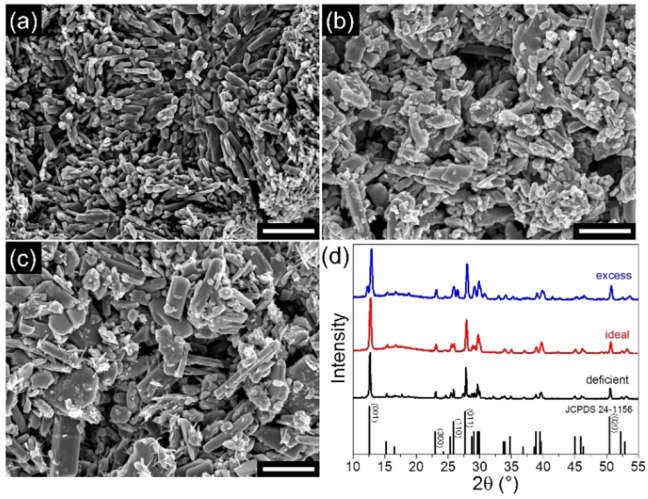

Figure 1. SEM micrographs of the $Na_xV_3O_8$ products with (a) deficient, (b) ideal, and (c) excess sodium stoichiometry where the scale bar in each image is equivalent to 2 μm. (d) Normalized XRD patterns.

demonstrates the profound effects that Na-content can have on morphology, homogeneity, and particle size distribution. The resulting particle morphology seems to shift from elongated nanoparticles with approximate width and thickness of 800 and 300 nm, respectively, to 900 nm long and 60 nm wide nanowires with increasing Na-content; correspondingly, the average particle size also decreases. It should be noted that the stoichiometric and excess sodium samples have a wider dispersion of particle morphology, where the elongated nanoparticle morphology is primarily maintained. The Na-deficient material (Figure 1a) has noticeable striations running along the edges that are apparent in the higher magnification images and are somewhat present in the images corresponding to the materials with higher Na-content, perhaps providing insight into the nanowire formation mechanism.

Quantitative elemental analysis was carried out using energy-dispersive X-ray spectroscopy (EDS), the results of which are tabulated and compared with their ideal values in Table 1. The experimentally determined sodium contents match incredibly well with the expected values based off of precursor quantities used during synthesis. These sodium compositions are accommodated by the formation of oxygen vacancies and partial transition metal reduction, and can be expressed as $Na_{1.25x}V_3O_{8-y}$ ($x < 1$) and $Na_{1.25x}V_zV_{3-z}O_8$ ($x > 1$) for the deficient and excess sodium compositions, respectively; the vanadium valence will be verified by XPS. These suppositions are substantiated by previous studies involving overstoichiometric Li_xCoO_2 samples, where it was deduced that the charge

DOI: 10.1021/acs.chemmater.5b02935
Chem. Mater. 2015, 27, 7082−7090

Table 2. Rietveld Refinement of $Na_xV_3O_8$ Products with Deficient, Stoichiometric, and Excess Sodium Stoichiometry

		lattice parameters				fit parameters		
sample	$Na_{1.25}V_3O_8$ phase (%)	a (Å)	b (Å)	c (Å)	β (deg)	χ^2	wRp	Rp
JCPDS 24-1156	100	7.32	3.61	12.14	106.73			
excess	94.4	7.28	3.62	12.18	106.99	2.02	0.09	0.06
stoichiometric	98.6	7.36	3.63	12.20	107.26	1.93	0.04	0.03
deficient	98.3	7.37	3.63	12.21	107.28	1.85	0.07	0.06

imbalance resulting from excess lithium is compensated by oxygen vacancies;[40] however, structural and electrostatic considerations should not be as overly influential in this system considering the *d*-electron configurations, affecting the formal valence state and covalent bonding interactions with the nearest-neighbor anions, of the cobalt and vanadium redox couples are disparate. Furthermore, Rietveld refinement was successively completed to ensure that the detected elemental sodium originates from $Na_xV_3O_8$ and not some vanadia derivative or sodium oxide impurity.

Following calcination, the crystal structure of the samples was analyzed and could be indexed to $Na_{1.25}V_3O_8$ phase (space group: $P2_1/m$ (11), JCPDS card 24-1156) via XRD, Figure 1d. Sodium trivanadate, $Na_{1+x}V_3O_8$, is a propitious positive electrode material for alkali-ion insertion because of its low cost, easy synthesis, and good electrochemical performance. This oxide has a layered structure, with the anionic V_3O_8 layers held together by alkali-ions, typically Li^+ or Na^+, distributed over two crystallographically independent sites, the interlayer octahedral as well as tetrahedral (but with lessened occupancy) sites.[41,42] The V_3O_8 framework is comprised of two structural units, namely double chains of edge-sharing VO_6 octahedra and double chains of edge-sharing trigonal bipyramids. These chains are linked by corner-shared oxygen that effectively form a continuously puckered sheet of VO_6 octahedra that comprise the stacked V_3O_8 strands. Sodium ions are situated between these quasilayers and form layers along the crystallographic [100] direction and double layers along the [001] direction. In this manner, the positively charged sodium ions electrostatically hold together the $[V_3O_8]^-$ strands. Additionally, there are several distorted octahedra that share faces with tetrahedra that form a two-dimensional interlinked tetrahedral-octahedral network that supports Na-ion transport between layers. The sodium ions have the inclination to serve as "pillar" cations by stabilizing the structure against volumetric changes during the (de)insertion processes of guest-ions at the vacant tetrahedral sites. There are six tetrahedral sites available per unit cell, in which excess sodium may be accommodated. Larger cations typically induce larger interlayer spacing values which can increase the diffusion rate and improve the dis/charge kinetics of the material and is evidenced by the higher Li-ion insertion ability of $Na_{1+x}V_3O_8$ than that in isostructural $Li_{1+x}V_3O_8$.[42,43] The structure can be likened to an analogue of the barnesite or metahewettite groups.[44−48]

Quantitative phase analysis was performed using Rietveld refinement (Table 2 and Figure S2 in SI) as to affirm the phase homogeneity of the various samples and detect any potential differences in the crystal lattices, primarily along the interlayer *c* direction. The monoclinic $Na_{1.25}V_3O_8$ phase was the predominant phase detected, with near complete phase composition for the deficient and stoichiometric Na-content samples based off the fitting results, and slightly reduced phase homogeneity for the excess Na-content specimen, which is to be expected on account of partial cation reduction; differences in the calculated interlayer *c* direction spacing were negligible. Analogous interlayer spacing values are reassuring as any variation in electrochemical performance can then be directly tied to defect states and is not dependent on structural disparities. Thus, SEM and Rietveld refinement have proven crucial in validating the purity and commensurable qualities of the differing samples and reinforce that any further distinctions among the various samples are rooted in chemical disparity prompted by means of the defect nature.

FTIR was conducted to distinguish the chemical nature and comparatively analyze the structural characteristics of the specimens with different Na-content, as shown in Figure 2a;

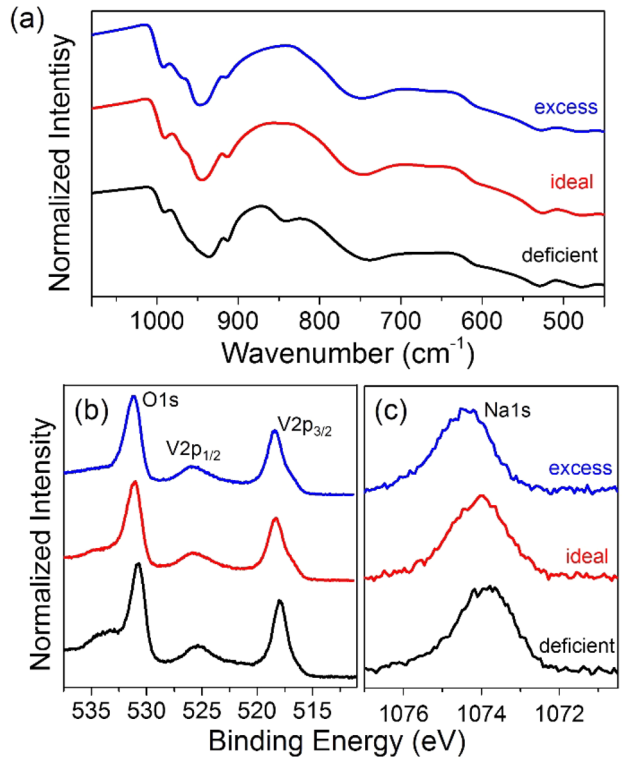

Figure 2. (a) FTIR, (b) V 2p/O 1s XPS, and (c) Na 1s XPS spectra of the $Na_xV_3O_8$ products with excess, ideal, and deficient sodium stoichiometry.

the absorption band values have been compiled in Table S1 in SI. The absorption bands stemming from the symmetric stretching mode of the vanadyl V═O bond is observed at approximately 991 and 944 cm^{-1} for all of the samples; the small inflections in the stoichiometric and excess Na content correspond to this mode as well. The 3-fold-coordinated oxygen asymmetric and symmetric stretching vibrations modes of V—O—V are represented by the bands localized at 745 and 527 cm^{-1}, respectively. The lack of sodium, or presence of oxygen vacancies, in the Na-deficient specimen appears to have

DOI: 10.1021/acs.chemmater.5b02935
Chem. Mater. 2015, 27, 7082−7090

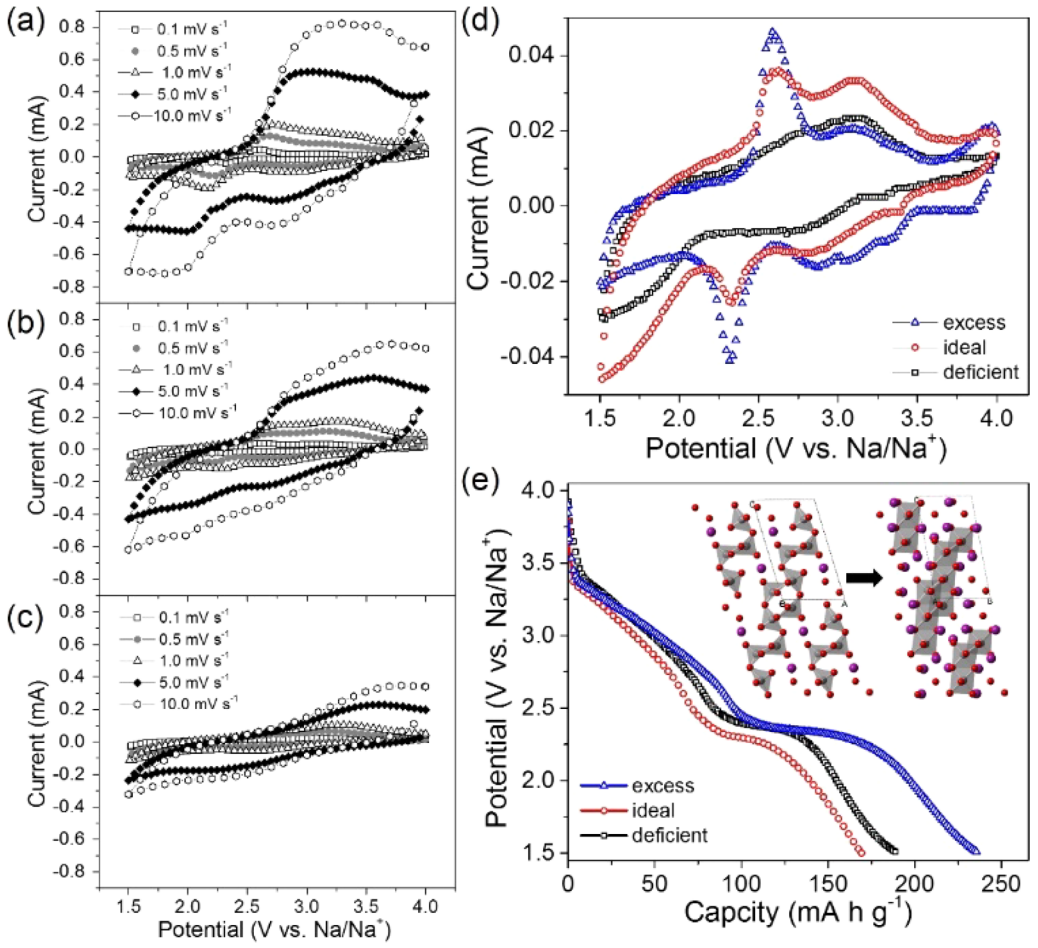

Figure 3. Cyclic voltammograms of $Na_xV_3O_8$ with (a) excess, (b) stoichiometric, and (c) deficient sodium content at different potential sweep rates of 0.1, 0.5, 1.0, 5.0, and 10.0 mV s^{-1} (from inner to the outer). (d) Direct comparison of cyclic voltammograms collected at 0.1 mV s^{-1} potential sweep rate and (e) initial full cycle discharge potential profiles of $Na_xV_3O_8$ products with different sodium content; inset shows schematic depiction of crystallographic changes undergone during sodiation.

its largest impact on this mode (Table S1 in SI). The 840 cm^{-1} band for the Na-deficient sample can be attributed to the coupled vibration between the V═O and V—O—V bonds but may be an artifact resulting from oxygen vacancies.[49,50]

XPS was carried out on the samples prior to electrochemical testing in order to obtain more information on the chemical state of the vanadium species present. High-resolution scans, emphasizing the V 2p and O 1s peaks, were collected and are shown in Figure 2b, whereas Figure 2c showcases the Na 1s results. The raw fitted scans are displayed in Figure S3 in SI. The trends between peak position, peak spacing, and their literature comparisons reveal that both the V $2p_{3/2}$ and O 1s orbital peak positions incrementally rose with sodium content. The V $2p_{3/2}$/O 1s peak positions for the deficient, stoichiometric, and excess Na samples were 530.8/517.9, 531.1/518.3, and 531.2/518.4 eV, respectively. The valence of the vanadium phase was confirmed to be predominately pentavalent as determined by the difference in binding energy between the V $2p_{3/2}$ and O 1s orbitals, which was approximately 12.8 eV for all of the analyzed specimens. The difference in binding energy ΔBE between the O 1s and V $2p_{3/2}$ level is commonly used to determine the oxidation state of vanadium oxides.[51−53] This was further corroborated by the V $2p_{3/2}$ and V $2p_{1/2}$ spin−orbit splitting of approximately 7.5 eV for all samples. These findings are consistent with literature reports.[54,55]

A noticeable shoulder on the low binding energy side of the V $2p_{3/2}$ peak for the stoichiometric and excess Na- content samples is indicative of a secondary vanadium species, namely V^{4+}. Previous studies have indicated that even in stoichiometric specimens, there is a slight preferential occupation of V^{4+} at preferential vanadium sites.[56] This is also expected as the ideal stoichiometry, $Na_{1.25}V_3O_8$, can only be achieved with the presence of some tetravalent vanadium species, but the comparison between the two is still valid because of their concentration differences. An additional feature of interest is the broad peak extending beyond the main O 1s peak in the 532.5 to 535 eV range for the Na-deficient sample that may be attributed to C—O(H).[51] The Na 1s peak for all samples is approximately 1074 eV, which is somewhat higher than typical literature values, and there is a clear shift toward higher BE concurrent with the sodium content.[54,57] The combination of EDX and XPS results tabulates the sodium contents (x in $Na_xV_3O_8$) for the deficient, stoichiometric, and excess specimens at 0.92 ± 0.01 ($Na_{0.92}V_3O_8$), 1.18 ± 0.05 ($Na_{1.18}V_3O_8$), and 1.42 ± 0.04 ($Na_{1.42}V_3O_8$), respectively.

Cyclic voltammograms of the $Na_xV_3O_8$ specimens with varying Na-content collected from sweep rates ranging from 0.1 to 10 mV s^{-1} are shown in Figure 3a−c, whereas a direct

DOI: 10.1021/acs.chemmater.5b02935
Chem. Mater. 2015, 27, 7082−7090

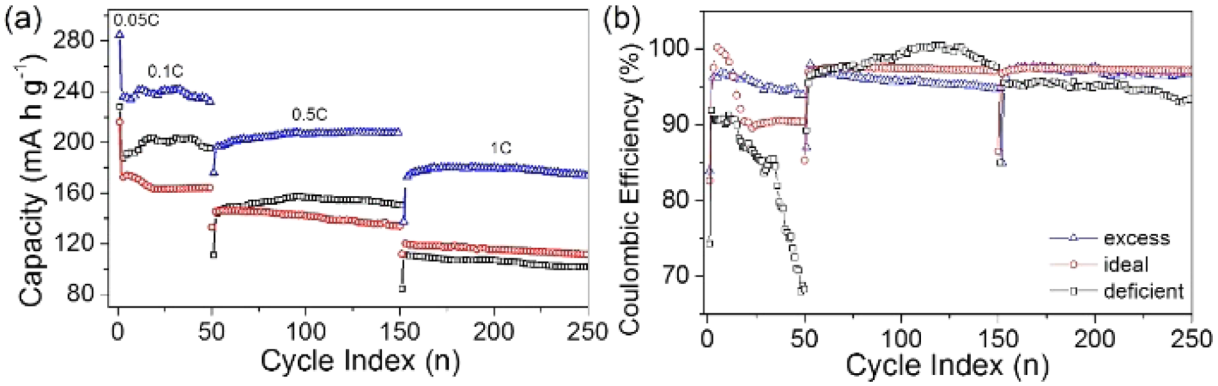

Figure 4. (a) Cycle stability and rate performance, and (b) Coulombic efficiency of $Na_{1+x}V_3O_8$ with deficient, stoichiometric, and excess sodium content.

comparison of the scans collected at a potential sweep rate of 1 mV s^{-1} are shown in Figure 3d. The peak magnitude and area of the redox peaks noticeably increase with the potential sweep rate, whereas the oxidation peaks and corresponding reduction peaks shifted to higher and lower potentials, respectively, due to polarization at the higher sweep rates. These features confirm the favorable charge transfer kinetics even at high potential sweep rates. The raw peaks and their locations show similarities that have previously been correlated with annealing temperature; specifically, the sodium content would appear to be inversely related to crystallinity.[58] However, this is known to not be the case as determined on the basis of Rietveld refinement.

A linear dependency between the anodic and cathodic peak currents and the square root of the potential sweep rate indicates that the sodiation process is limited by solid state diffusion in the host material. If the rate-limiting step is sodium diffusion in the electrode and the charge transfer at the interface is fast enough, the relationship between the peak current and the CV scan rate can be expressed by the Randles–Sevcik equation[59]

$$I_p = (2.69 \times 10^5) n^{3/2} A C_{Na}^* D_{Na}^{1/2} \nu^{1/2} \quad (2)$$

where I_p, n, A, and ν are the peak current, number of exchanged electrons, surface area of the electrode, and potential sweep rate; D_{Na} is the sodium ion chemical diffusion coefficient and C_{Na}* is the bulk concentration of sodium (0.011 mol cm^{-3} for $Na_xV_3O_8$ derived from the theoretical density of 3.55 g cm^{-3}).[60] The average value of D_{Na} into the $Na_xV_3O_8$ samples of deficient, ideal, and excess sodium stoichiometry is calculated to be 3.05, 1.53, and 1.89 × 10^{-14} cm^2 s^{-1}, respectively. The improved diffusion coefficients of the deficient and excess sodium content materials in comparison to the ideal stoichiometry show that Na diffusion is highly dependent on the local environment and configurations of Na ions, and Na–Na interactions through association.[61]

All electrodes were electrochemically tested in the Na-ion half-cell configuration, and assuming a theoretical capacity of 350 mA h g^{-1} corresponding to the total incorporation of four Na^+ per $[V_3O_8]$ formula unit. The initial current density was 17.5 mA g^{-1} (0.05C) so as to produce a stable cathode-electrolyte interface, or cathode solid electrolyte interphase (SEI) analogue. Following this, the cells were cycled at 35 (0.1C), 175 (0.5C), and 350 (1.0C) mA g^{-1} for 50, 100, and 100 cycles, respectively. The potential discharge profiles from the first complete cycle collected at 35 mA g^{-1} are shown collectively in Figure 3e, with the schematic inset illustrating the change in crystal structure upon sodiation up to $Na_4V_3O_8$. The overall discharge profiles are very similar to the only real differences being the onset and duration of the potential plateau. The $Na_xV_3O_8$ cells with deficient, stoichiometric, and excess Na-content delivered initial discharge capacities of 189, 169, and 235 mA h g^{-1}, respectively.

The cycle stability, rate performance, and Coulombic efficiency (CE) of the deficient, stoichiometric, and excess Na-content $Na_xV_3O_8$ cells are also displayed in Figure 4a,b and depict a fairly different story than originally expected based off the discharge profiles. Subsequent cycles at 0.1C saw somewhat erratic capacity values and stability issues as discerned through the CE. This was most apparent for the oxygen vacancy containing $Na_xV_3O_8$ electrode as the CE dropped from 91 to 66%; there were similar preliminary issues for the pristine $Na_xV_3O_8$ electrode, which seemed to stabilize and reach an equilibria with successive cycling, whereas the mixed cation (Na-excess) electrode showed comparatively stable capacities and the highest CE of 96%. The deficient, stoichiometric, and excess Na-content $Na_xV_3O_8$ cell capacities respectively dropped to 150, 145, and 201 mA h g^{-1} and then again to 112, 121, and 180 mA h g^{-1} when the discharge current was increased to 175 and 350 mA g^{-1}.

The CE values were markedly more stable at these increased current densities as well. The Na-deficient electrode still exhibited some stability issues as observed through the CE and the strikingly larger drops in capacity, as compared to the other electrodes, accompanying increases in current density. The pristine electrode material actually overtook the Na-deficient electrode in terms of capacity and CE at the 1.0C rate. The initially enhanced capacity of the crystalline matrix populated with vacancies can be attributed to weaker Na–O bond strength that accelerates Na hopping between occupied and vacant oxygen sites. However, the ordering of oxygen framework is eventually induced as a result of either transition metal or sodium diffusion in an attempt to reduce the structural free energy.[9] The vacancies order into channels that are easily accessible for sodium ion intercalation, but this eventually leads to capacity retention and stability issues as revealed through prolonged cycling.[62,63] Fell et al. recently showed that for the $Li[Ni_xLi_{(1/3)-(2x/3)}Mn_{(2/3)-(x/3)}]O_2$ (x = 1/5) structure, micro-strain can originate from a lithium deficient structure (point defects and vacancies) and that there are multiple phenomena occurring in the bulk such as transition metal migration as well as oxygen loss.[9] This has further been corroborated by

DOI: 10.1021/acs.chemmater.5b02935
Chem. Mater. 2015, 27, 7082–7090

experimental studies showing that the presence of oxygen vacancies can lead to the loss of domain order and capacity fading due to structural collapse, and a similar mechanism may play a role in the performance seen here.[64]

Electronic localization has been directly observed in other layered transition metal oxides—directly affirming that the exhibited electronic properties are strongly correlated to the Na-ion distribution in the interlayer space.[65] Thus, the cationic distribution of the individual samples could differ significantly since the sodium content levels are unequal. On a more global level, the cationic distribution is comprised of: electrostatic repulsions between the individual Na-ions along the interlayer *c* axis, Na^+—V^{5+} repulsion occurring through the common face of the VO_6 polyhedra, as well as the intraelectron interactions within the vanadium layers. For any given system, the cationic distribution will seek to reach a minimum. Thus, the cationic distribution is highly sensitive to the sodium content as it can have serious impact on the constituent influences. A slight change in sodium composition may be enough to induce the formation of an entirely new cationic distribution.[66]

Electron transport has been demonstrated to be affected strongly by solid—solution formation and, correspondingly, other means of introduced atomic-level disorder.[67] Consequently, the structure of excess sodium-containing $Na_xV_3O_8$ lends itself to both favorable mass and electronic charge transport. The excess sodium bolsters the mechanical integrity of the layered structure itself, whereas the Na^+ in the original lattice gives way to additional metal—oxygen bonds other than V—O. This ultimately reduces the number of sp^3 orbitals of oxygen available for bonding with the incoming sodium-ions, and the interaction between tetrahedrally coordinated Na^+ and O^{2-} is weak enough to grant fast movement of sodium from site to site.[68,69] Based purely on electrostatic considerations, it would be expected that $Na_xV_3O_8$ with excess sodium would suffer from low-migration energy given that the sodium sites generate strong electrostatic repulsion on one another. The activation of such forces would induce high migration energy barriers. Moreover, Na-ion ordering or structuring would also be anticipated to negatively impact sodium diffusion in a substantial manner provided the considerable effect of Na—Na interactions on the local Na migration energy. However, cationic mixing poses a route of overcoming these deficiencies by potentially perturbing the ordering of the transition metal sublattice, which would consequently result in a weaker Na ordering and thereby improve sodium diffusion. The defected (disordered) materials consistently delivered higher capacities than the more ordered (pristine) counterpart, clearly demonstrating the critical role of structural ordering on kinetics.

CONCLUSIONS

In the present work, we successfully synthesized defective $Na_xV_3O_8$ where it was possible to control the dominant defect type through sodium stoichiometry manipulation. Thus, Na-deficiency leads to the formation of oxygen vacancies and Na-excess leads to partial cation reduction, or the formation of a cation disordered structure. When examined as NIB electrode material, the superior performance of the Na-excess, cation disordered, materials was clearly revealed, especially at higher current discharge densities. The formation of oxygen vacancies initially seemed promising, but was coupled with stability issues and capacity fading with further cycling. The disparity in electrochemical performance was attributed to variations in the electronic distribution as promoted through Na-ion interactions and the direct influence of such on the oxygen framework (sublattice); these factors were determined to have significant impact on the migration energy and diffusion barriers. This study provides insight on defect and stoichiometry considerations for cathode materials and provides a potential mechanism toward significantly improving the performance of rechargeable alkali-ion batteries.

ASSOCIATED CONTENT

Supporting Information

The Supporting Information is available free of charge on the ACS Publications website at DOI: 10.1021/acs.chemmater.5b02935.

Additional TGA, N_2 sorption analyses, Rietveld refinement, FTIR, XPS, and electrochemical data. (PDF)

AUTHOR INFORMATION

Corresponding Author

*E-mail: gzcao@u.washington.edu.

Notes

The authors declare no competing financial interest.

ACKNOWLEDGMENTS

This research work has been financially supported in part by the National Science Foundation (CMMI-1030048, DMR-1505902) and the University of Washington TGIF grant. Part of this work was conducted at the University of Washington NanoTech User Facility, a member of the NSF National Nanotechnology Infrastructure Network (NNIN). This material is based in part upon work supported by the State of Washington through the University of Washington Clean Energy Institute.

REFERENCES

(1) Hudak, N.; Huber, D. Nanostructured Lithium-Aluminum Alloy Electrodes for Lithium-Ion Batteries. *ECS Trans.* **2010**, *33*, 1—13.

(2) Mikkor, M. Graphite Aluminum and Silicon Carbide Coated Current Collectors for Sodium-Sulfur Cells. *J. Electrochem. Soc.* **1985**, *132*, 991—998.

(3) Slater, M. D.; Kim, D.; Lee, E.; Johnson, C. S. Sodium-Ion Batteries. *Adv. Funct. Mater.* **2013**, *23*, 947—958.

(4) Lee, J.; Urban, A.; Li, X.; Su, D.; Hautier, G.; Ceder, G. Unlocking the Potential of Cation-Disordered Oxides for Rechargeable Lithium Batteries. *Science* **2014**, *343*, 519—522.

(5) Uchaker, E.; Zheng, Y. Z.; Li, S.; Candelaria, S. L.; Hu, S.; Cao, G. Z. Better than crystalline: amorphous vanadium oxide for sodium-ion batteries. *J. Mater. Chem. A* **2014**, *2*, 18208—18214.

(6) Li, Y.; Yao, J.; Uchaker, E.; Zhang, M.; Tian, J.; Liu, X.; Cao, G. Sn-Doped V_2O_5 Film with Enhanced Lithium-Ion Storage Performance. *J. Phys. Chem. C* **2013**, *117*, 23507—23514.

(7) Liu, D.; Liu, Y.; Pan, A.; Nagle, K. P.; Seidler, G. T.; Jeong, Y.-H.; Cao, G. Enhanced Lithium-Ion Intercalation Properties of V_2O_5 Xerogel Electrodes with Surface Defects. *J. Phys. Chem. C* **2011**, *115*, 4959—4965.

(8) Carroll, K. J.; Qian, D.; Fell, C.; Calvin, S.; Veith, G. M.; Chi, M.; Baggetto, L.; Meng, Y. S. Probing the electrode/electrolyte interface in the lithium excess layered oxide $Li_{1.2}Ni_{0.2}Mn_{0.6}O_2$. *Phys. Chem. Chem. Phys.* **2013**, *15*, 11128—11138.

(9) Fell, C. R.; Qian, D.; Carroll, K. J.; Chi, M.; Jones, J. L.; Meng, Y. S. Correlation Between Oxygen Vacancy, Microstrain, and Cation Distribution in Lithium-Excess Layered Oxides During the First Electrochemical Cycle. *Chem. Mater.* **2013**, *25*, 1621—1629.

DOI: 10.1021/acs.chemmater.5b02935
Chem. Mater. 2015, 27, 7082—7090

(10) Qian, D.; Xu, B.; Chi, M.; Meng, Y. S. Uncovering the roles of oxygen vacancies in cation migration in lithium excess layered oxides. *Phys. Chem. Chem. Phys.* **2014**, *16*, 14665−14668.
(11) Song, J.; Shin, D. W.; Lu, Y.; Amos, C. D.; Manthiram, A.; Goodenough, J. B. Role of Oxygen Vacancies on the Performance of $Li[Ni_{0.5-x}Mn_{1.5+x}]O_4$ (x = 0, 0.05, and 0.08) Spinel Cathodes for Lithium-Ion Batteries. *Chem. Mater.* **2012**, *24*, 3101−3109.
(12) Sushko, P. V.; Rosso, K. M.; Zhang, J.-G.; Liu, J.; Sushko, M. L. Oxygen Vacancies and Ordering of d-levels Control Voltage Suppression in Oxide Cathodes: the Case of Spinel $LiNi_{0.5}Mn_{1.5}O_{4-\delta}$. *Adv. Funct. Mater.* **2013**, *23*, 5530−5535.
(13) Bazant, M. Z. Theory of Chemical Kinetics and Charge Transfer based on Nonequilibrium Thermodynamics. *Acc. Chem. Res.* **2013**, *46*, 1144−1160.
(14) Singh, G. K.; Ceder, G.; Bazant, M. Z. Intercalation dynamics in rechargeable battery materials: General theory and phase-transformation waves in $LiFePO_4$. *Electrochim. Acta* **2008**, *53*, 7599−7613.
(15) Zhu, H. Y.; Lan, Y.; Gao, X. P.; Ringer, S. P.; Zheng, Z. F.; Song, D. Y.; Zhao, J. C. Phase Transition between Nanostructures of Titanate and Titanium Dioxides via Simple Wet-Chemical Reactions. *J. Am. Chem. Soc.* **2005**, *127*, 6730−6736.
(16) Wang, X. H.; Li, J. G.; Kamiyama, H.; Katada, M.; Ohashi, N.; Moriyoshi, Y.; Ishigaki, T. Pyrogenic Iron(III)-Doped TiO_2 Nanopowders Synthesized in RF Thermal Plasma: Phase Formation, Defect Structure, Band Gap, and Magnetic Properties. *J. Am. Chem. Soc.* **2005**, *127*, 10982−10990.
(17) Mizushima, K.; Jones, P. C.; Wiseman, P. J.; Goodenough, J. B. Li_xCoO_2 (0 < x<-1): A new cathode material for batteries of high energy density. *Mater. Res. Bull.* **1980**, *15*, 783−789.
(18) Duncan, H.; Hai, B.; Leskes, M.; Grey, C. P.; Chen, G. Relationships between Mn^{3+} Content, Structural Ordering, Phase Transformation, and Kinetic Properties in $LiNi_xMn_{2-x}O_4$ Cathode Materials. *Chem. Mater.* **2014**, *26*, 5374−5382.
(19) Jo, M. R.; Kim, Y.-I.; Kim, Y.; Chae, J. S.; Roh, K. C.; Yoon, W.-S.; Kang, Y.-M. Lithium-Ion Transport through a Tailored Disordered Phase on the $LiNi_{0.5}Mn_{1.5}O_4$ Surface for High-Power Cathode Materials. *ChemSusChem* **2014**, *7*, 2248−2254.
(20) Lee, E.; Persson, K. A. Solid-Solution Li Intercalation as a Function of Cation Order/Disorder in the High-Voltage $Li_xNi_{0.5}Mn_{1.5}O_4$ Spinel. *Chem. Mater.* **2013**, *25*, 2885−2889.
(21) Shin, D. W.; Bridges, C. A.; Huq, A.; Paranthaman, M. P.; Manthiram, A. Role of Cation Ordering and Surface Segregation in High-Voltage Spinel $LiMn_{1.5}Ni_{0.5-x}M_xO_4$ (M = Cr, Fe, and Ga) Cathodes for Lithium-Ion Batteries. *Chem. Mater.* **2012**, *24*, 3720−3731.
(22) Xiao, J.; Chen, X.; Sushko, P. V.; Sushko, M. L.; Kovarik, L.; Feng, J.; Deng, Z.; Zheng, J.; Graff, G. L.; Nie, Z.; Choi, D.; Liu, J.; Zhang, J.-G.; Whittingham, M. S. High-Performance $LiNi_{0.5}Mn_{1.5}O_4$ Spinel Controlled by Mn^{3+} Concentration and Site Disorder. *Adv. Mater.* **2012**, *24*, 2109−2116.
(23) Lee, E.; Persson, K. A. Revealing the coupled cation interactions behind the electrochemical profile of $LixNi_{0.5}Mn_{1.5}O_4$. *Energy Environ. Sci.* **2012**, *5*, 6047−6051.
(24) Fang, H.-T.; Liu, M.; Wang, D.-W.; Sun, T.; Guan, D.-S.; Li, F.; Zhou, J.; Sham, T.-K.; Cheng, H.-M. Comparison of the rate capability of nanostructured amorphous and anatase TiO2 for lithium insertion using anodic TiO2 nanotube arrays. *Nanotechnology* **2009**, *20*, 225701.
(25) Kim, Y.; Park, Y.; Choi, A.; Choi, N. S.; Kim, J.; Lee, J.; Ryu, J. H.; Oh, S. M.; Lee, K. T. An amorphous red phosphorus/carbon composite as a promising anode material for sodium ion batteries. *Adv. Mater.* **2013**, *25*, 3045−9.
(26) Venkatesh, G.; Pralong, V.; Lebedev, O. I.; Caignaert, V.; Bazin, P.; Raveau, B. Amorphous sodium vanadate Na(1.5+y)VO3, a promising matrix for reversible sodium intercalation. *Electrochem. Commun.* **2014**, *40*, 100−102.
(27) Xiong, H.; Slater, M. D.; Balasubramanian, M.; Johnson, C. S.; Rajh, T. Amorphous TiO2 Nanotube Anode for Rechargeable Sodium Ion Batteries. *J. Phys. Chem. Lett.* **2011**, *2*, 2560−2565.
(28) Paudel, T. R.; Zakutayev, A.; Lany, S.; d'Avezac, M.; Zunger, A. Doping Rules and Doping Prototypes in A_2BO_4 Spinel Oxides. *Adv. Funct. Mater.* **2011**, *21*, 4493−4501.
(29) Kilner, J. A.; Brook, R. J. A study of oxygen ion conductivity in doped non-stoichiometric oxides. *Solid State Ionics* **1982**, *6*, 237−252.
(30) Luo, J.-Y.; Chen, L.-J.; Zhao, Y.-J.; He, P.; Xia, Y.-Y. The effect of oxygen vacancies on the structure and electrochemistry of $LiTi_2(PO_4)_3$ for lithium-ion batteries: A combined experimental and theoretical study. *J. Power Sources* **2009**, *194*, 1075−1080.
(31) Chung, S.-Y.; Bloking, J. T.; Chiang, Y.-M. Electronically conductive phospho-olivines as lithium storage electrodes. *Nat. Mater.* **2002**, *1*, 123−128.
(32) Dahéron, L.; Martinez, H.; Dedryvère, R.; Baraille, I.; Ménétrier, M.; Denage, C.; Delmas, C.; Gonbeau, D. Surface Properties of $LiCoO_2$ Investigated by XPS Analyses and Theoretical Calculations. *J. Phys. Chem. C* **2009**, *113*, 5843−5852.
(33) Murakami, M.; Noda, Y.; Koyama, Y.; Takegoshi, K.; Arai, H.; Uchimoto, Y.; Ogumi, Z. Local Structure and Spin State of Cobalt Ion at Defect in Lithium Overstoichiometric $LiCoO_2$ As Studied by $^{6/7}Li$ Solid-State NMR Spectroscopy. *J. Phys. Chem. C* **2014**, *118*, 15375−15385.
(34) Hong, S. Y.; Kim, Y.; Park, Y.; Choi, A.; Choi, N.-S.; Lee, K. T. Charge carriers in rechargeable batteries: Na ions vs. Li ions. *Energy Environ. Sci.* **2013**, *6*, 2067−2081.
(35) Datta, D.; Li, J.; Shenoy, V. B. Defective Graphene as a High-Capacity Anode Material for Na- and Ca-Ion Batteries. *ACS Appl. Mater. Interfaces* **2014**, *6*, 1788−1795.
(36) Clark, J. M.; Barpanda, P.; Yamada, A.; Islam, M. S. Sodium-ion battery cathodes $Na_2FeP_2O_7$ and $Na_2MnP_2O_7$: diffusion behaviour for high rate performance. *J. Mater. Chem. A* **2014**, *2*, 11807−11812.
(37) Toby, B. H. EXPGUI, a graphical user interface for GSAS. *J. Appl. Crystallogr.* **2001**, *34*, 210−213.
(38) Liu, H.; Zhou, H.; Chen, L.; Tang, Z.; Yang, W. Electrochemical insertion/deinsertion of sodium on NaV6O15 nanorods as cathode material of rechargeable sodium-based batteries. *J. Power Sources* **2011**, *196*, 814−819.
(39) Lee, C. Y.; Marschilok, A. C.; Subramanian, A.; Takeuchi, K. J.; Takeuchi, E. S. Synthesis and characterization of sodium vanadium oxide gels: the effects of water (n) and sodium (x) content on the electrochemistry of $Na_{(x)}V_2O_5$ (n)H_2O. *Phys. Chem. Chem. Phys.* **2011**, *13*, 18047−54.
(40) Levasseur, S.; Ménétrier, M.; Shao-Horn, Y.; Gautier, L.; Audemer, A.; Demazeau, G.; Largeteau, A.; Delmas, C. Oxygen Vacancies and Intermediate Spin Trivalent Cobalt Ions in Lithium-Overstoichiometric $LiCoO_2$. *Chem. Mater.* **2002**, *15*, 348−354.
(41) de Picciotto, L. A.; Adendorff, K. T.; Liles, D. C.; Thackeray, M. M. Structural characterization of $Li_{1+x}V_3O_8$ insertion electrodes by single-crystal X-ray diffraction. *Solid State Ionics* **1993**, *62*, 297−307.
(42) Wadsley, A. D. Crystal Chemistry of Non-stoichiometric Pentavalent Vanadium Oxides: Crystal Structure of $Li_{1+x}V_3O_8$. *Acta Crystallogr.* **1957**, *10*, 261−267.
(43) Nguyen, D.; Gim, J.; Mathew, V.; Song, J.; Kim, S.; Ahn, D.; Kim, J. Plate-Type NaV_3O_8 Cathode by Solid State Reaction for Sodium-Ion Batteries. *ECS Electrochem. Lett.* **2014**, *3*, A69−A71.
(44) Evans, H. T., Jr; Hughes, J. M. Crystal chemistry of the natural vanadium bronzes. *Am. Mineral.* **1990**, *75*, 508−521.
(45) Evans, H. T. The crystal structure of hewettite. *Can. Mineral.* **1989**, *27*, 181−188.
(46) Barnes, W. H. Hewettite and Metahewettite. *Am. Mineral.* **1955**, *40*, 689−691.
(47) Frost, R. L.; Erickson, K. L.; Weier, M. L. Hydrogen bonding in selected vanadates: a Raman and infrared spectroscopy study. *Spectrochim. Acta, Part A* **2004**, *60*, 2419−2423.
(48) Frost, R. L.; Erickson, K. L.; Weier, M. L.; Carmody, O. Raman and infrared spectroscopy of selected vanadates. *Spectrochim. Acta, Part A* **2005**, *61*, 829−834.
(49) Fu, H.; Jiang, X.; Yang, X.; Yu, A.; Su, D.; Wang, G. Glycothermal synthesis of assembled vanadium oxide nanostructures

DOI: 10.1021/acs.chemmater.5b02935
Chem. Mater. 2015, 27, 7082−7090

for gas sensing. *J. Nanopart. Res.* **2012**, *14*, 1−14, DOI: 10.1007/s11051-012-0871-z.
(50) Ragupathy, P.; Shivakumara, S.; Vasan, H. N.; Munichandraiah, N. Preparation of Nanostrip V2O5 by the Polyol Method and Its Electrochemical Characterization as Cathode Material for Rechargeable Lithium Batteries. *J. Phys. Chem. C* **2008**, *112*, 16700−16707.
(51) Silversmit, G.; Depla, D.; Poelman, H.; Marin, G. B.; De Gryse, R. Determination of the V2p XPS binding energies for different vanadium oxidation states (V^{5+} to V^{0+}). *J. Electron Spectrosc. Relat. Phenom.* **2004**, *135*, 167−175.
(52) Mendialdua, J.; Casanova, R.; Barbaux, Y. XPS studies of V_2O_5, V_6O_{13}, VO_2 and V_2O_3. *J. Electron Spectrosc. Relat. Phenom.* **1995**, *71*, 249−261.
(53) Demeter, M.; Neumann, M.; Reichelt, W. Mixed-valence vanadium oxides studied by XPS. *Surf. Sci.* **2000**, *454−456*, 41−44.
(54) Tang, Y.; Sun, D.; Wang, H.; Huang, X.; Zhang, H.; Liu, S.; Liu, Y. Synthesis and electrochemical properties of NaV_3O_8 nanoflakes as high-performance cathode for Li-ion battery. *RSC Adv.* **2014**, *4*, 8328−8334.
(55) Yu, J.; Yu, J. C.; Ho, W.; Wu, L.; Wang, X. A Simple and General Method for the Synthesis of Multicomponent $Na_2V_6O_{16}\cdot 3H_2O$ Single-Crystal Nanobelts. *J. Am. Chem. Soc.* **2004**, *126*, 3422−3423.
(56) Schindler, M.; Hawthorne, F. C.; Alexander, M. A.; Kutluoglu, R. A.; Mandaliev, P.; Halden, N. M.; Mitchell, R. H. Na−Li−$[V_3O_8]$ insertion electrodes: Structures and diffusion pathways. *J. Solid State Chem.* **2006**, *179*, 2616−2628.
(57) He, H.; Jin, G.; Wang, H.; Huang, X.; Chen, Z.; Sun, D.; Tang, Y. Annealed NaV_3O_8 nanowires with good cycling stability as a novel cathode for Na-ion batteries. *J. Mater. Chem. A* **2014**, *2*, 3563.
(58) Liang, S.; Chen, T.; Pan, A.; Liu, D.; Zhu, Q.; Cao, G. Synthesis of $Na_{1.25}V_3O_8$ nanobelts with excellent long-term stability for rechargeable lithium-ion batteries. *ACS Appl. Mater. Interfaces* **2013**, *5*, 11913−7.
(59) Bard, A. J.; Faulkner, L. R. *Electrochemical Methods: Fundamentals and Applications*; Wiley: Weinheim, Germany, 2000.
(60) Heli, H.; Yadegari, H.; Jabbari, A. Investigation of the Lithium Intercalation Behavior of Nanosheets of LiV_3O_8 in an Aqueous Solution. *J. Phys. Chem. C* **2011**, *115*, 10889−10897.
(61) Mo, Y.; Ong, S. P.; Ceder, G. Insights into Diffusion Mechanisms in P2 Layered Oxide Materials by First-Principles Calculations. *Chem. Mater.* **2014**, *26*, 5208−5214.
(62) Xiong, H.; Yildirim, H.; Shevchenko, E. V.; Prakapenka, V. B.; Koo, B.; Slater, M. D.; Balasubramanian, M.; Sankaranarayanan, S. K. R. S.; Greeley, J. P.; Tepavcevic, S.; Dimitrijevic, N. M.; Podsiadlo, P.; Johnson, C. S.; Rajh, T. Self-Improving Anode for Lithium-Ion Batteries Based on Amorphous to Cubic Phase Transition in TiO_2 Nanotubes. *J. Phys. Chem. C* **2012**, *116*, 3181−3187.
(63) Huang, R.; Ikuhara, Y. H.; Mizoguchi, T.; Findlay, S. D.; Kuwabara, A.; Fisher, C. A. J.; Moriwake, H.; Oki, H.; Hirayama, T.; Ikuhara, Y. Oxygen-Vacancy Ordering at Surfaces of Lithium Manganese(III,IV) Oxide Spinel Nanoparticles. *Angew. Chem., Int. Ed.* **2011**, *50*, 3053−3057.
(64) Hao, X.; Lin, X.; Lu, W.; Bartlett, B. M. Oxygen Vacancies Lead to Loss of Domain Order, Particle Fracture, and Rapid Capacity Fade in Lithium Manganospinel ($LiMn_2O_4$) Batteries. *ACS Appl. Mater. Interfaces* **2014**, *6*, 10849−10857.
(65) Huang, Q.; Foo, M. L.; Lynn, J. W.; Zandbergen, H. W.; Lawes, G.; Wang, Y.; Toby, B. H.; Ramirez, A. P.; Ong, N. P.; Cava, R. J. Low temperature phase transitions and crystal structure of $Na_{0.5}CoO_2$. *J. Phys.: Condens. Matter* **2004**, *16*, 5803.
(66) Berthelot, R.; Carlier, D.; Delmas, C. Electrochemical investigation of the P2−Na_xCoO_2 phase diagram. *Nat. Mater.* **2011**, *10*, 74−80.
(67) Tang, M.; Carter, W. C.; Chiang, Y.-M. Electrochemically Driven Phase Transitions in Insertion Electrodes for Lithium-Ion Batteries: Examples in Lithium Metal Phosphate Olivines. *Annu. Rev. Mater. Res.* **2010**, *40*, 501−529.
(68) Pistoia, G.; Panero, S.; Tocci, M.; Moshtev, R. V.; Manev, V. Solid solutions $Li_{1+x}V_3O_8$ as cathodes for high rate secondary Li batteries. *Solid State Ionics* **1984**, *13*, 311−318.
(69) Hong, H. Y. P. Solid electrolytes containing both mobile and immobile alkali ions. *J. Power Sources* **1980**, *5*, 137−142.

DOI: 10.1021/acs.chemmater.5b02935
Chem. Mater. 2015, 27, 7082−7090